Theory to predict particle migration and margination in the pressure-driven channel flow of blood

Qin M. Qi and Eric S. G. Shaqfeh[*]

Department of Chemical Engineering, Stanford University, Stanford, California 94305, USA

The inhomogeneous concentration distribution of erythrocytes and platelets in microchannel flows particularly in directions normal to the mean flow plays a significant role in hemostasis, drug delivery, and microfluidic applications. In this paper, we develop a coarse-grained theory to predict these distributions in pressure-driven channel flow at zero Reynolds number and compare them to experiments and simulations. We demonstrate that the balance between the deformability-induced lift force and the shear-induced diffusion created by hydrodynamic interactions in the suspension results in both a peak concentration of red blood cells at the channel center and a cell-free or Fahraeus-Lindqvist layer near the walls. On the other hand, the absence of a lift force and the strong red blood cell-platelet interactions result in an excess concentration of platelets in the cell-free layer. We demonstrate a strong role of hematocrit (i.e., erythrocyte volume fraction) in determining the cell-free layer thickness and the degree of platelet margination. We also demonstrate that the capillary number of the erythrocytes, based on the membrane shear modulus, plays a relatively insignificant role in the regimes that we have studied. Our theory serves as a good and simple alternative to large-scale computer simulations of the cross-stream transport processes in these mixtures.

I. INTRODUCTION

As is well known, blood is a biological fluid mixture containing, among many other entities, red blood cells (RBCs), platelets, and white blood cells suspended in plasma. Each species not only differs in its biological function, but also exhibits a unique inhomogeneous concentration distribution normal to the mean flow direction in the blood circulation. These concentrations change nonmonotonically with the distance to the walls of either a blood vessel or a microfluidic channel and are not easily understood using simple shear-induced diffusion models. In the case of red blood cells flowing through capillary tubes, the histogram of their distribution obtained from experiments typically shows a concentration peak at the centerline [1], usually a number of off-center peaks, and finally a cell-free Fahreus-Lindqvist layer at the wall [2]. A number of these characteristics (e.g., the cell-free layer) of red blood cell flow are not observed for rigid particles in Poiseuille flow [3], and are commonly referred to as the characteristics of red blood cell migration. Platelets, on the other hand, are depleted from the cell-laden region and become concentrated in the cell-free layer [1,4]. Nanoparticles and microparticles of various shapes show distributions similar to that of platelets in blood suspensions [5–8], and we refer to this phenomenon as particle margination. Red blood cell migration plays a direct role in reducing the effective viscosity of blood [9,10] and controlling plasma skimming [11]. In addition, platelet margination occurs only in the presence of red blood cells, and is apparently important in hemostasis [12] and thrombosis formation [13]. As has been discussed by numerous researchers [14–16], there is thus a great significance in studying cell migration, particle margination, and their relationship in order to understand the human biology of blood.

---

[*]Also at Mechanical Engineering, Stanford University and Institute for Computational and Mathematical Engineering, Stanford University.

Red blood cell deformability plays a key role in migration by generating a lift force acting away from the wall [17], thus distinguishing the cross-flow movement of cells from that of rigid particles. Experiments have demonstrated that the stationary aspherical shape of red blood cells [18] is no longer maintained under pressure-driven flow [19]. The lack of a nucleus in red blood cells simplifies their structures, and thus they are a good model of passive deformable particles. The factors controlling their deformation are apparent when one notes that red blood cells have an amphiphilic bilayer membrane encapsulating an internal fluid, as well as an internal spectrin network for additional mechanical strength [20,21]. Their resistance to deformation is therefore governed by the interplay between the lipid bilayer and the cytoskeleton [22]. A local reduction in red blood cell concentration and thus a cell-free layer as described above, is formed by flow near surfaces when the lift force dominates other forces acting on the cell. Diseased cells, such as those with sickle cell disease or malaria, are found to have weak lifting forces and thus a reduced cell-free layer thickness [21,23,24]. Since red blood cells occupy a volume fraction between 40% and 50% in a given arterial flow [25], they can be considered as the dominant flow species and their distribution thus has great impact on the dynamics of other blood particles.

On the other hand, platelets occupy a volume fraction of less than 1% in flowing blood, and therefore their distribution is largely influenced by interactions with red blood cells as opposed to their self-interactions. Because of their relative inflexibility and nonactivated shape, freely flowing platelets are often treated as rigid discoid-shaped particles. As the hematocrit increases, Fitzgibbon *et al.* found enhanced margination of platelet-sized rigid spheres in flowing blood [15], as characterized by a concentration peak, which both moves closer to the wall and increases in magnitude as hematocrit is increased. Mehrabadi *et al.* [26] measured the effective diffusivity of platelets in blood and showed that platelets undergo RBC-enhanced shear-induced diffusion. In the case of a wall trauma, platelets must first travel normal to the mean flow direction, reach the bleeding site on the wall, and begin the formation of a platelet plug near the trauma site. Therefore, it is advantageous to have marginated platelets in the vicinity of the vessel wall to reduce the time associated with the early stages of clot formation.

Beyond understanding the microhydrodynamics of blood flow within the blood vessels, it is well known that the commercial value of blood-based medical devices is greatly determined by the amount of blood used, and thus microfluidic devices because of their compact size may be preferred. In these devices, blood flows through channels with the smallest dimension being O $(10\,\mu\text{m})$, and margination and migration phenomena are key features of the physical functioning of the device. In this context, Fitzgibbon *et al.* [15] estimated that the entrance length of microparticle margination in flowing blood was approximately 1 cm in a channel of width of 30 μm. In a variety of applications, researchers [27–31] have utilized varying degrees of cell migration to perform cell sorting based on size and deformability and remove unwanted components of blood. *In vitro* studies of marginated platelets adhering to reactive surfaces in channel flow serve as a dynamic assay to predict cardiovascular diseases [32]. In drug delivery applications, particles ranging from O $(1\,\mu\text{m})$ to O $(10\,\text{nm})$ have been examined as drug carriers and their degree of margination is considered a key factor influencing the delivery efficiency to the vicinity of target sites [5,6,33,34].

Numerous simulation studies have been completed to understand the motion of flowing red blood cells and platelets or rigid particles using a variety of techniques including boundary integral methods [14,35,36], immersed boundary simulations [37], and dissipative particle dynamics [38,39]. These simulations confirm the observations made in early experiments that red blood cell migration is a deformability-induced phenomenon and particle margination is a result of the less concentrated and less deformable particles interacting with the dominant cell species. However, the inclusion of all particle species in simulations of whole blood always requires large-scale computing that is expensive and time consuming. Moreover, each change of a single design parameter, e.g., the size of the dilute, rigid particles, requires a new set of simulations even though the dominant cell species is essentially unaffected.

In the past decade, researchers have renewed interest in developing approximate theories for the flow of deformable particle suspensions particularly after sufficient information was gleaned

from both experiments and simulations. Thus, using analogous methods that have previously been pioneered for determining the rigid particle distribution in channel flows [40,41], theories have been developed for both droplet migration [42] as well as capsule and red blood cell migration [39,43–47] in channel and tube flows all with the inclusion of wall-induced lift. The flow field in these theories is usually approximated (at least locally) as simple shear flow for convenience [39,44–46], and the resulting concentration profile of the deformable species is characterized by a peak near the wall and a plateau at the centerline. Therefore, they fail to reproduce the concentration peak at the centerline as observed in experiments [1] and simulations [14,48]. Despite this apparent discrepancy, most researchers argue that their simple shear flow approximation can capture the cell-free layer thickness correctly. For example, Katanov and coworkers [39] used a balance between particle pressure due to shear-induced diffusion and surface pressure due to hydrodynamic lift to obtain an estimate for the cell-free layer thickness in the limit of small capillary number. They examined the effects of the hematocrit, the capillary number and the tube radius on the cell-free layer thickness. However, the agreement is only qualitative in small tubes. The latest contribution to this field is a theory by Rivera *et al.* [47]. They considered the scenario of a pressure-driven flow in channels and used a simplified expression for shear-induced diffusion and hydrodynamic lift to obtain analytical solutions for particle distributions. They argued that based on the relative magnitude of each cross-flow contribution, different migration and margination profiles can be achieved. These idealized models certainly help describe the fundamental physics governing margination and migration. However, none of the existing work is able to achieve a quantitative, or even semiquantitative agreement with experimental and simulation results.

In this paper, we propose a theory that allows the prediction of the red blood cell and platelet distribution normal to the mean flow direction in pressure-driven flow using results from fast, small-scale (i.e., one or two particle) simulations and a collision-based Boltzmann equation approach. Similar to the previous work [45,47], we identify shear-induced diffusion and deformability-induced lift as two major flux contributions governing the cross-flow transport in blood. Finally, since rigid spheres follow a similar margination mechanism as that of platelets, we include predictions for the margination of spheres of different sizes. The novelty of our work lies in (i) resolving issues unique to pressure-driven flow due to shear rate gradients; (ii) modeling the membrane properties and asphericity of red blood cells using the Skalak law [49]; (iii) explicitly calculating shear-induced diffusional flux based on particle pair interactions; and (iv) comparing with simulation and experimental results for quantitative verification. Our goal is to develop a lower-dimensional model that accelerates the computation of margination and migration in these systems while maintaining high accuracy in the results. This model can be used not only to understand the fundamental physics in the transport of blood, but also to guide the design of microfluidic devices.

II. MODEL DESCRIPTION

A. Overview

Our work is focused on the flow of blood through rectangular channels. A schematic of the flow is shown in Fig. 1. We denote x as the flow direction, y as the vorticity direction and z as the direction of the velocity gradient. We consider wall effects only in the z direction and ignore variations in the y direction. Thus our flow can be approximated as a two-dimensional channel flow. The smallest dimension z has a height H being approximately $10\,\mu$m. This size matches human arterioles and venules as well as a typical dimension of microfluidic devices. We consider a binary suspension of red blood cells and platelets in plasma. Red blood cells are treated as aspherical deformable particles while platelets are rigid discoids. A pressure gradient over the channel in the x direction is supplied to drive the flow. Plasma is treated as a Newtonian fluid, and therefore we would expect a parabolic flow profile on the x-z plane in the absence of red blood cells. The existence of red blood cells makes the mean flow profile more blunt and therefore increases the actual wall shear rate at a constant mean flow [50]. Our goal is to determine the number density of red blood cells n_C and platelets n_P
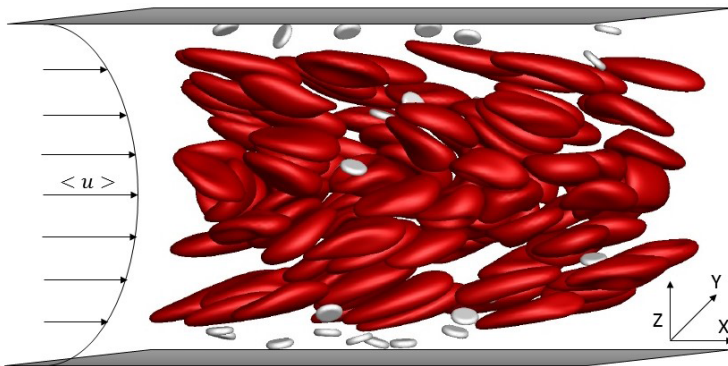
FIG. 1. A schematic of red blood cells (red) and platelets (white) in wall-bound channel flow driven by a pressure gradient.

at steady state as a function of z. n_P will later be generalized to the number density of rigid spheres. We consider n_C and n_P as functions of z only. In our theory, we make the following assumptions.

(i) We assume the Reynolds number is low (i.e., $\mathrm{Re} = \frac{\rho \dot{\gamma}_c H^2}{\mu} \ll 1$, where $\dot{\gamma}_c$ is the characteristic shear rate. ρ and μ are the plasma density and viscosity) such that inertial effects are ignored and we can apply Stokes flow theories.

(ii) We ignore Brownian motion in the dynamics of red blood cells and platelets (i.e., the corresponding Peclet number $\mathrm{Pe} = \frac{6\pi \mu \dot{\gamma}_c r^3}{k_B T} \to \infty$, where r is the particle radius, k_B is the Boltzmann constant and T is the temperature). However, we do consider this effect for smaller rigid spheres.

(iii) Red blood cells are assumed to be in the dilute to semidilute concentration regime, such that two-cell interactions dominate. Platelets and rigid spheres are much more dilute than red blood cells, and thus three-body or more interactions can be ignored completely. Also, hydrodynamic interactions in the nondilute regime are reduced significantly by intermediate scattering events, as demonstrated by detailed simulations [51,52]. Therefore, we can utilize such enhanced decay of hydrodynamic interactions to simplify our calculation.

(iv) We assume the behavior of particles in blood suspension can be approximated by their behavior in pure plasma. Specifically, we assume the behavior of a single red blood cell lifting in a blood suspension can be approximated by its behavior in the absence of other particles. We also assume the dynamics of two particles interacting in a blood suspension can be approximated by their interactions in pure plasma. We will later present the comparison between our theory and full-scale simulations to justify this assumption.

The last assumption is the key in our theory such that we replace the simulation of hundreds of particles with the simulation of only one or two particles in order to dramatically decrease computation time. In general our theory can be extended to the study of general suspensions of deformable particles (e.g., vesicles and capsules) and rigid particles as long as the assumptions above are satisfied.

We consider three types of motion that govern the cross-flow distributions of red blood cells and particles: (i) hydrodynamic "collisions" and fluctuations, (ii) hydrodynamic lift, and (iii) Brownian motion. We describe the physics of each type of motion below.

(i) *Hydrodynamic "collisions" and fluctuations*. In channel flow under shear, hydrodynamic interactions between two aspherical particles moving towards each other lead to changes in particle trajectories. The result is an increase in the cross-flow distance between the pair of particles. The rate at which two particles interact scales linearly with the velocity difference between the two and therefore is a shear-induced phenomenon. In the case of such a collision where two particles are of the same type, this change in distance after successive collisions has a diffusive effect, or creates so-called shear-induced diffusion as first discovered by Leighton and Acrivos [40]. The hematocrit

Ht for the channel sizes we have chosen ranges from 10% to 20%, and is lower than the whole blood hematocrit, but is characteristic of the hematocrit in small blood vessels due to branching effects [53]. While many previous studies on simple shear flow include the assumption that three-body effects and higher are negligible for these hematocrits [35,45–47], we consider these higher-order effects in our work by introducing an additional hydrodynamic diffusivity D (i.e., as an add on to the explicit consideration of two-body collisions) to determine the size of these multibody effects for suspensions of red blood cells.

(ii) *Hydrodynamic lift*. At zero Reynolds number, deformable particles experience a lift force away from the wall in pressure-driven flow. This tendency to migrate creates a convective flux away from the wall. The lift forces from opposite walls drive the cells towards the centerline of the channel. This lift force is induced by the wall due to the interaction of the deformable particle with its image stresslet as well as the shear rate gradient in pressure-driven flow [54–56].

(iii) *Brownian motion*. As mentioned in assumption (ii), we ignore Brownian motion for red blood cells and platelets since Pe $> 10^4$. We consider Brownian motion for rigid microspheres and nanospheres since they are much smaller than red blood cells. D_B denotes Brownian diffusivity for such particles and it contributes a diffusive flux to their distribution. We consider $D_B = \frac{k_B T}{6\pi \mu r} = 3.6 \times 10^{-11} m^2/s$ for a nanosphere 10 nm in diameter, which corresponds to Pe $= 0.001$. Notice that in the hydrodynamic collisions, we do not include Brownian motion and assume that the particle displacements are of the same magnitude as those for bigger particles. Thus, we assume that the shear rate is high and the Peclet number is large for the collision process.

B. Master equations

We start with the governing equations for red blood cell concentration, n_C, and platelet concentration, n_P, in the form of advection-diffusion equations as follows:

$$\frac{\partial n_C}{\partial t} + \frac{\partial (u_{lift} n_C)}{\partial z} + \frac{\partial F_{CC}}{\partial z} - \frac{\partial}{\partial z}\left(D \frac{\partial n_C}{\partial z}\right) = 0 \tag{1}$$

$$\frac{\partial n_P}{\partial t} + \frac{\partial F_{CP}}{\partial z} + \frac{\partial F_{PP}}{\partial z} - \frac{\partial}{\partial z}\left(D_B \frac{\partial n_P}{\partial z}\right) = 0. \tag{2}$$

u_{lift} is the lift velocity of red blood cells, D is the hydrodynamic diffusivity of red blood cells and D_B is the Brownian diffusivity of rigid spheres. F_{CC}, F_{CP}, and F_{CP} denote the fluxes created by cell-cell collisions, cell-platelet collisions, and platelet-platelet collisions, respectively. We ignore the effect of platelet-cell collisions on red blood cells due to the relative paucity of platelets. Thus the distribution of red blood cells is decoupled from that of platelets as shown in Eq. (1). At steady state, we first determine the distribution of red blood cells by balancing lift and collisional fluxes and thereafter we obtain the distribution of platelets using Eq. (2) by setting $D_B = 0$. In the end, we consider the case of rigid spheres where $F_{PP} = 0$ and D_B is nonzero. Over a long period of time($t \gg t_{coll}$), we assume binary collisions are memoryless and shear-induced diffusion can be treated as a Markovian process [57]. Thus, the collisional fluxes can be written as follows:

$$F_{CC} = \int_{\delta_z} \int_{\delta_y} \int_0^{\Delta_{CC}} n_C(z-b) n_C(z-b-\delta_z) \delta u \, db \, d\delta_y \, d\delta_z \tag{3a}$$

$$F_{PP} = \int_{\delta_z} \int_{\delta_y} \int_0^{\Delta_{PP}} n_P(z-b) n_P(z-b-\delta_z) \delta u \, db \, d\delta_y \, d\delta_z \tag{3b}$$

$$F_{CP} = \int_{\delta_z} \int_{\delta_y} \int_0^{\Delta_{CP}} n_P(z-b) n_C(z-b-\delta_z) \delta u \, db \, d\delta_y \, d\delta_z. \tag{3c}$$

In the above expressions, δ_y and δ_z are the initial separation distances between two particles in the y and z directions. We will impose a cutoff distance R on these interactions as the upper
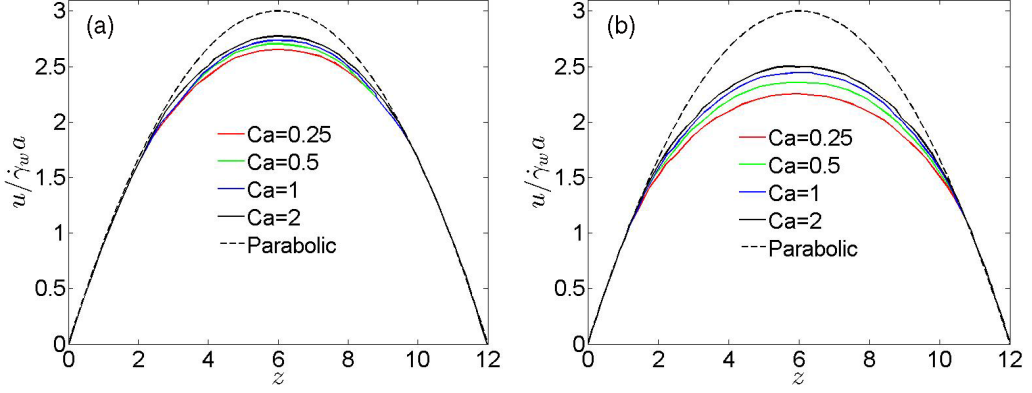
FIG. 2. The mean velocity in the x flow direction (solid lines) and the ideal parabolic flow velocity (dashed lines), with both normalized by the wall shear velocity. $L_z = 12$ ($H = 33.8 \, \mu$m). (a) Ht = 10%, (b) Ht = 20%. Ca $= \frac{\mu \dot{\gamma}_c a}{E_s}$, where E_s is the cell membrane shear modulus. Reprinted with permission [14].

limit on δ_y and δ_z. The value of R will be determined from simulations in the following section. In the presence of a shear rate gradient, hydrodynamics interactions are usually asymmetric during a collision, even for two particles of the same species, leading to different displacement values for two particles. Δ_{CC}, Δ_{PP}, and Δ_{CP} are the cross-flow displacement values of the second particle due to hydrodynamic interactions or collisions. δu is the relative velocity difference between two particles in the x direction.

In the continuum model above, we are concerned with only center-of-mass distributions. One obvious drawback is the zero collisional flux at the centerline due to vanishing shear rate. In addition, the lift flux decays to zero at the centerline due to symmetry. Thus, the zero net flux causes an aphysical singularity issue that does not exist in the solution for simple shear flow. We adopt the approach of Miller and Morris [3] of adding a nonlocal shear rate correction term κ to the local center-of-mass shear rate $\dot{\gamma}_0(z)$: $\dot{\gamma}(z) = \dot{\gamma}_0(z) + \kappa \dot{\gamma}_c/2$. We examine this effect for $\kappa = 1, \epsilon, \epsilon^2$, where $\epsilon = 2a/H$ and a is the equivalent radius of red blood cells. This correction takes into account the finite size of particles such that they sample shear rates around their volume and therefore the particle as a whole never experiences zero net shear rate. For a fixed $\dot{\gamma}_c$, an increase in H also reduces the value of ϵ due to the reduction in the range of shear rates surrounding the particle. Thus, $\delta u = \delta u_0 + \kappa \dot{\gamma}_c \delta_z/2$, where δu_0 is the center-of-mass velocity difference. As can be seen from Fig. 2, the actual velocity profile of red blood cells at steady state deviates from a parabolic velocity profile. Therefore, the velocity profile depends on the distribution of red blood cells to be determined. However, this effect diminishes as hematocrit decreases and channel size increases. To simplify the equation to be solved, we reference the actual red blood cell velocity profile from simulations [6,14] as seen on Fig. 2 and calculate δu_0.

Three sets of inputs are required to solve the master equations (1) and (2) at steady state: the red blood cell lift velocity u_{lift}, displacement values from binary collisions Δ_{CC}, Δ_{PP}, Δ_{CP}, and the hydrodynamic diffusivity D for red blood cells. Rivera $et\ al.$ wrote down similar master equations. However, these values are not determined explicitly. Instead, they examined the relative contribution of lift and binary collisions over a wide range of values [47,58]. In the present work, we explicitly calculate the magnitude of each quantity. Thus, we are taking a bottom-up approach to examine the mechanism of migration and margination, which is an important distinction from the previous work. The lift velocity has been determined for drops and vesicles in Poiseuille flow [59,60]. We utilize boundary integral simulations to determine u_{lift} vs. z for a single red blood cell. The displacement values for drops [61], red blood cells [45], and capsules [35] in simple shear flow have been characterized, but we are not aware of any literature on red blood cell hydrodynamic collisions in pressure-driven flow. We determine displacement values Δ from two-particle simulations. The

hydrodynamic diffusivity is a lumped parameter for many-body collisional displacements. This diffusivity varies with z as $D = \bar{D}a^2\dot{\gamma}(z)$ due to shear-induced diffusion. We will use $\bar{D}$ as a fitting parameter to increase the accuracy of our results in terms of cell-free layer thickness l when comparing to whole blood simulations—thus examining the effect of higher order multibody interactions in determining the concentration distribution.

To solve these master equations, we discretize the z direction into $2N + 1$ equally spaced intervals. Therefore, the concentrations can be expressed as: $n_C(z) = \sum_{j=1}^{N} a_j \xi_j(z)$ and $n_P(z) = \sum_{j=1}^{N} b_j \xi_j(z)$. $\xi_j(z)$ are piecewise linear shape functions with a mesh size of $1/16$ cell radius. We then take an inner product of the master equations at steady state with these shape functions:

$$\left\langle \xi_i(z), u_{lift} n_C + F_{CC} - D\frac{\partial n_C}{\partial z} \right\rangle = 0 \tag{4}$$

$$\left\langle \xi_i(z), F_{CP} + F_{PP} - D_B\frac{\partial n_P}{\partial z} \right\rangle = 0. \tag{5}$$

Our numerical approach is similar to that outlined for simple shear flow [45]. Due to symmetry, we solve a system of N quadratic equations for each species, subject to the total volume fraction constraint.

$$\sum_{j=1}^{N} U_{ij}a_j + \sum_{j=1}^{N}\sum_{m=1}^{N} f_{CC,ijm}a_j a_m - \sum_{j=1}^{N} d_{ij}a_j = 0 \tag{6}$$

$$\sum_{j=1}^{N}\sum_{m=1}^{N} f_{CP,ijm}b_j a_m + \sum_{j=1}^{N}\sum_{m=1}^{N} f_{PP,ijm}b_j b_m - \sum_{j=1}^{N} d_{B,ij}b_j = 0 \tag{7}$$

$$U_{ij} = \langle \xi_i(z), u_{lift}(z)\xi_j(z) \rangle \quad d_{ij} = \left\langle \xi_i(z), D(z)\frac{\xi_j(z)}{z} \right\rangle$$

$$f_{AB,ijm} = \left\langle \xi_i(z), \int_{\delta_z} \int_{\delta_y} \int_0^{\Delta_{AB}} \xi_j(z-b)\xi_m(z-b-\delta_z)\delta u \, db \, d\delta_y \, d\delta_z \right\rangle.$$

All integral expressions above are evaluated using the midpoint rule in intervals that are 0.05 times cell radius. Using a uniform density profile as our initial guess, the coefficients a_i and b_i can be determined using Newton's iteration.

C. Boundary integral method

As mentioned above, our theory does rely on simulation outputs, which are red blood cell lift velocity u_{lift} and collisional displacements Δ_{CC}, Δ_{PP}, and Δ_{CP}. We utilize an existing boundary integral simulation method [14,62] that determines the dynamics of red blood cells and platelets at zero Reynolds number. Instead of simulating the whole suspension as shown in Fig. 1, we reduce the number of particles to one or two as necessary for the inputs to the Boltzmann theory.

As mentioned in Sec. I, red blood cell membranes are nearly incompressible phospholipids supported by a spectrin network. This structure offers red blood cells the resistance to shear, dilatation, and bending. We model the shear elasticity using the Skalak law [49]. The typical volume of a red blood cell is $V_C = 94 \, \mu\text{m}^3$ [63], which corresponds to an equivalent radius of $a = 2.82 \, \mu\text{m}$ [14]. The shear modulus is found to range between 6–9 μN/m [64], the bending modulus E_B is typically 2–4×10^{-19} J and the dilatational modulus is 480 mN/m [65]. Therefore, we set the dilatational modulus to be $100 \, \mu\dot{\gamma}_C a$, which creates less than 1% change of area in each surface mesh element and thus ensures near incompressibility. The bending modulus is set to $E_B = 3.3 \times 10^{-3}a^2 E_S$ and is included primarily to suppress buckling. The reduced volume ν
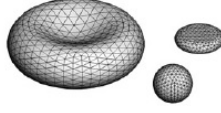
FIG. 3. Surface meshes and reference shapes used for a red blood cell, a platelet, and a rigid sphere in boundary integral simulations.

($\nu = \frac{3\sqrt{4\pi}V_C}{S^{\frac{3}{2}}}$, where S is the surface area) is kept at 0.65, corresponding to a highly aspherical shape since $\nu = 1$ for a perfect sphere. The membrane properties listed above create the biconcave shape of red blood cells at rest as seen in Fig. 3. The viscosity ratio λ is the ratio of the internal to external fluid viscosity. The physiological value of λ is about 5. At such viscosity ratio, a single red blood cell undergoes a rigid-body-like tumbling motion in flow while red blood cells in a suspension at finite concentration exhibit tank-treading behavior. Narsimhan [45] studied the effect of the viscosity ratio on the cell-free layer thickness in a single cell simulation in simple shear flow by solving an equation similar to Eq. (1). He showed that $\lambda = 1$ results agree more closely with experimental data than $\lambda = 5$. Therefore, we choose a viscosity ratio $\lambda = 1$ in our simulations such that we can recover the tank-treading behavior seen in blood suspensions. We model platelets as rigid oblates with a diameter of 2.8 μm and a thickness of 0.7 μm. Similar to red blood cells, platelets and spheres have surfaces discretized as triangular meshes as seen in Fig. 3.

Our boundary integral simulation contains three types of equations that solve for RBC membrane velocity u_C, wall friction force $[\![\mathbf{f}_W]\!]$, and a double-layer density on platelet or sphere surface $\boldsymbol{\psi}_P$. The details of the simulation are identical to Zhao *et al.* [14] unless specified otherwise. In the case of cell-only simulations, rigid body motions are no longer considered while cell contributions are ignored in platelet-platelet simulations. Thus the actual equations solved are much simpler.

The full boundary integral equations on the red blood cells, platelets, and walls are

$$\frac{1+\lambda}{2}\mathbf{u}_C - u_\infty = \frac{1-\lambda}{8\pi}\mathbf{K}_{CC}\mathbf{u}_C - \frac{1}{8\pi\mu}\mathbf{N}_{CC}[\![\mathbf{f}_C]\!] - \frac{1}{8\pi}\mathbf{K}_{CP}\boldsymbol{\psi}_P - \frac{1}{8\pi\mu}\mathbf{N}_{CW}[\![\mathbf{f}_W]\!] \quad (8a)$$

$$\frac{1}{2}\boldsymbol{\psi}_P - u_\infty = -\sum_{\beta=1}^{6}(\mathbf{q}^{''\beta},\boldsymbol{\psi}_P)\mathbf{q}^{''\beta} + \frac{1-\lambda}{8\pi}\mathbf{K}_{PC}\mathbf{u}_C - \frac{1}{8\pi\mu}\mathbf{N}_{PC}[\![\mathbf{f}_C]\!]$$

$$- \frac{1}{8\pi}\mathbf{K}_{PP}\boldsymbol{\psi}_P - \frac{1}{8\pi\mu}\mathbf{N}_{PW}[\![\mathbf{f}_W]\!] \quad (8b)$$

$$0 = \frac{1-\lambda}{8\pi}\mathbf{K}_{WC}\mathbf{u}_C - \frac{1}{8\pi\mu}\mathbf{N}_{WC}[\![\mathbf{f}_C]\!] - \frac{1}{8\pi\mu}\mathbf{N}_{WW}[\![\mathbf{f}_W]\!] - \frac{1}{8\pi}\mathbf{K}_{WP}\boldsymbol{\psi}_P, \quad (8c)$$

where u_∞ is the far-field velocity of Poiseuille flow, and $\mathbf{q}^{''\beta}$ are the six independent modes of rigid body motion. The single- and double-layer kernels $\mathbf{N}$ and $\mathbf{K}$ are defined as:

$$(\mathbf{N}[\![f]\!])_j(\mathbf{x}_0) = \int [\![f]\!]_i(\mathbf{x})G_{ij}(\mathbf{x},\mathbf{x}_0)dS(\mathbf{x}) \quad (9)$$

$$(\mathbf{K}\mathbf{u})_j(\mathbf{x}_0) = \int \mathbf{u}_i(\mathbf{x})T_{ijk}(\mathbf{x},\mathbf{x}_0)\mathbf{n}_k(\mathbf{x})dS(\mathbf{x}) \quad (10)$$

and $\mathbf{G}$ and $\mathbf{T}$ are the fundamental Green's function solutions for the Stokeslet and stresslet with periodic boundary conditions [66]. The smooth particle mesh Ewald sum technique [67] is used to accelerate the simulation.
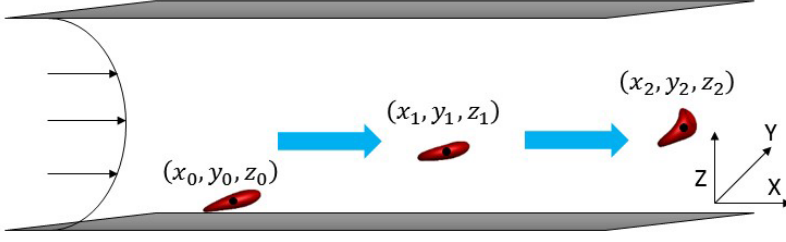
FIG. 4. Snapshot of a single red blood cell lift simulation.

D. Simulation domain

We choose the equivalent radius of a red blood cell $a = 2.82 \, \mu$m as our characteristic length scale. Our simulation domain is a three-dimensional rectangular box with a size of (L_x, L_y, L_z). We set $L_x = 32$, $L_y = 9$. We consider two values for L_z: 12 and 17.73 corresponding to $H = 33.84 \, \mu$m and 50 μm channels that match the sizes used in previous simulations or experiments [6,14]. We impose periodic boundary conditions in the x and y directions and no-slip boundary conditions in the z direction. Therefore, we consider a pressure-driven flow bound between two walls at $z = 0$ and $z = L_z$, respectively. We specify an average far-field flow velocity $\langle u \rangle$, corresponding to a parabolic velocity profile in the absence of particles: $u^\infty = 6 \langle u \rangle \frac{z(H-z)}{H^2}$. We define the capillary number as $\text{Ca} = \frac{\mu \dot{\gamma}_c a}{E_s}$, where the plasma viscosity μ is 1.2 cP and where the capillary number represents the ratio of viscous forces to red blood cell shear elastic forces. The characteristic shear rate $\dot{\gamma}_c = \frac{6 \langle u \rangle}{H}$ is defined as the equivalent wall shear rate in parabolic flow corresponding to the average flow velocity $\langle u \rangle$. For Ca $= 1$ the corresponding $\dot{\gamma}_c = 2000 \, \text{s}^{-1}$, comparable to arteriole wall shear rates [53]. As mentioned previously, the presence of red blood cells make the velocity profile more blunt and thus the actual wall shear rate $\dot{\gamma}_w$ is greater than $\dot{\gamma}_c$. Zhao *et al.* compared $\dot{\gamma}_w$ and $\dot{\gamma}_c$ in a 33.84 μm channel [14], and found the difference to be at most 20% when Ht $= 20\%$ and Ca $= 0.25$. This difference is less significant for higher capillary numbers and for a 50 μm channel. We vary the flow velocity to study the single cell hydrodynamic lift and two particle collisions over a range of Ca.

In the lift simulations, we place a red blood cell at a height $z_0 = h$ above the bottom wall in pressure-driven flow and time step the simulation as shown in Fig. 4 until the cell reaches the centerline of the channel. The cell's center-of-mass position is tracked over time and we can calculate $u_{lift} = dz/dt$ from this trajectory. Due to flow curvature, the local shear rate $\dot{\gamma}_0$ is a function of position z, which depends on t during the lift process. Therefore, instead of nondimensionalizing t with a constant characteristic wall shear rate $\dot{\gamma}_c$, we use the nondimensionalization in Eq. (11) to consider the history of shear rate variation and plot z vs. t^*.

$$t^* = \int_0^t \dot{\gamma}_0(t') dt' \tag{11}$$

In the collision simulations, we consider three types of hydrodynamic interactions independently: (i) cell-cell collisions, (ii) cell-platelet collisions and, finally, (iii) platelet-platelet collisions. For each type of interaction, we place the first particle at position $(L_x/2, L_y/2, z_0)$ and the second particle at position $(L_x/2 + \delta_x, L_y/2 + \delta_y, z_0 - \delta_z)$. Δ_{CC}, Δ_{PP}, and Δ_{PP} are functions of δ_y, δ_z, and z, where z is defined in terms of the particle's final position. We vary δ_y and δ_z as in our previous study in simple shear flow [45] until these initial separations are large enough that interactions are negligible. We also vary z since the shear rate is a function of z. For type (i) and (iii) collisions, we only need to vary z_0 from 0 to $L_z/2$ with $\delta_x, \delta_y, \delta_z > 0$ due to symmetry. For type (ii) collisions, z_0 varies from 0 to L_z with $\delta_x, \delta_y > 0$. For $0 < z < L_z/2$, $\delta_z > 0$ and for $L_z/2 < z < L_z$, $\delta_z < 0$. From now on, we refer to the particle initially closer to the wall as the near-wall particle and the other particle as the near-center particle. As shown in Fig. 5, we time step the simulation and record the trajectories of both particles over time. Red blood cells experience the lift force while colliding with other particles.
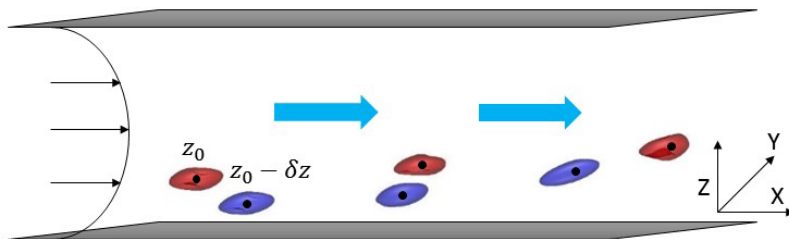
FIG. 5. Snapshot of a cell-cell collision simulation: the near-center red blood cell (red) starts at height z_0 and the near-wall red blood cell (blue) starts at height $z_0 - \delta_z$.

Therefore we subtract the simulated lift trajectory starting from the same initial position in order to obtain the contribution from hydrodynamic collisions only. After a sufficiently long time, two particles reach steady-state positions in the z direction. As mentioned before, these hydrodynamic interactions are irreversible and the particles generally will not return to their initial positions. Thus, the first particle will end up in $z = z_0 + \Delta z_1$ while the second particle at $z = z_0 - \delta_z - \Delta z_2$. The collisional displacements Δz_1 and Δz_2 can be calculated and their magnitudes are used in the collisional flux calculation. In our study, δ_y, δ_z, and z_0 are varied in equal intervals. The resulting Δz values can thus be tabulated in terms of δ_y, δ_z and z. We can quickly access Δ values at any given δ_y, δ_z, and z from interpolation in those three dimensions.

III. RESULTS: BOUNDARY INTEGRAL SIMULATIONS

A. Lift simulations

The trajectories of a single red blood cell lifting at Ca $= 0.25, 0.5, 1, 2$ are presented in Figure 6. By nondimensionalizing time as in Eq. (11), curves at different capillary numbers collapse, which agrees with findings from vesicle experiments [60]. The slopes of such curves represent the lift velocity scaled by the local shear rate $\dot{\gamma}_0(z) = \dot{\gamma}_c \bar{\gamma}_0(z)$ and are independent of the capillary number. Therefore, the dimensionless u_{lift} scales linearly with $\bar{\gamma}_0$. For the range of capillary numbers we are
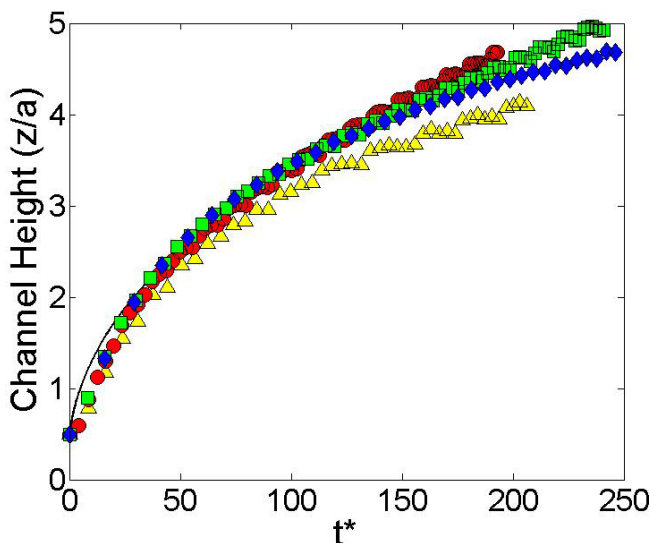

FIG. 6. Red blood cell lift trajectories from simulations, $L_z = 12$ ($H = 33.8\,\mu$m), Ca $= 0.25$ (yellow triangle), 0.5 (red sphere), 1 (green square), 2 (blue diamond), and fitted trajectory for Ca $= 1$ (black line).

TABLE I. Fitted values of lift velocity parameters from simulations.

L_z	Ca	ξ	α
12	0.25	0.055	1.3
12	0.5	0.057	1.0
12	1	0.069	1.3
12	2	0.087	1.6
17.73	0.25	0.045	1.2
17.73	0.5	0.031	1.3
17.73	1	0.039	1.2
17.73	2	0.048	1.2
Vesicle experiments [60]		0.012 ± 0.002	1 ± 0.1

considering, red blood cells reach a saturated shape due to membrane incompressibility and undergo tank-treading motion with some oscillation [68,69]. Deviations in shape occur mostly in the center region due to the reduction in shear rate. Therefore, we express the dimensionless lift velocity as follows:

$$u_{lift} = \frac{\xi \bar{\dot{\gamma}}_0(z)}{z^\alpha}. \tag{12}$$

The fitted line using Eq. (12) matches the lifting trend nicely. The fitted values for the coefficient ξ and powers α are tabulated in Table I. On average, the correlation for lift velocity is $u_{lift} = \frac{0.067 \bar{\dot{\gamma}}_0(z)}{z^{1.3}}$ for $L_z = 12$ and $u_{lift} = \frac{0.041 \bar{\dot{\gamma}}_0(z)}{z^{1.2}}$ for $L_z = 17.73$. Coupier *et al.* noted that the fitted coefficients depend only on reduced volume ν, and weakly on the channel height L_z and the capillary number Ca [60], which is consistent with our findings. Our fitted α values are also close to their fitted values for vesicles whose reduced volume $0.815 < \nu < 0.990$. The ξ values are not comparable due to the different scalings used. Similar to red blood cells, vesicles are deformable particles with incompressible membranes and were found to undergo tank-treading motion in the experiments for a viscosity ratio $\lambda = 1$ [60]. Therefore, it is not surprising that red blood cells resemble vesicles in terms of their lift velocity. There exists abundant literature on the lift velocity of vesicles [54,70–73] and red blood cells [69,74] in simple shear flow. In all those studies, it is straightforward to use the argument that the far-field velocity scales with $\frac{S_{zz}}{z^2}$ using the method of images. The two-wall contribution can be treated as a superposition of the lift velocity in opposite directions: $u_{lift} = K(\frac{1}{z^2} - \frac{1}{(L_z - z)^2})$. Thus, we would expect a faster decay than S_{zz}/z^2 due to the canceling effect from the opposite wall. In our case of Poiseuille flow, however, the correlation with z is lower than quadratic order, meaning the lift velocity decays more slowly with the wall distance z. This follows since the lift force arises from both the wall effect as well as the curvature of flow [75,76]. The curvature is significant especially near the centerline of the channel as compared to a simple, linear wall-induced lift, which obviously vanishes at the centerline due to zero shear rate. A previous vesicle simulation [60] has demonstrated that curvature-induced migration forces dominate over wall effects for $8 \leqslant z \leqslant L_z - 8$ when $L_z \geqslant 16$. This curvature provides a lift force even in the absence of the wall [56,76] and results from the interplay between particle shape and shear gradient [59]. The contribution from the opposite wall is also trivial compared to the curvature effect as shown by the α values obtained. Thus, the channel width does not significantly affect the lift velocity, which is consistent with our simulation results. As far as we are aware, the literature on the red blood cell lift velocity in pressure-driven flow is very limited [76]. We demonstrate that there are noticeable differences in the lift velocity away from the wall in pressure-driven flow. Therefore, our results are novel and valuable especially for interpreting experiments that examine and utilize the lift of a red blood cell.
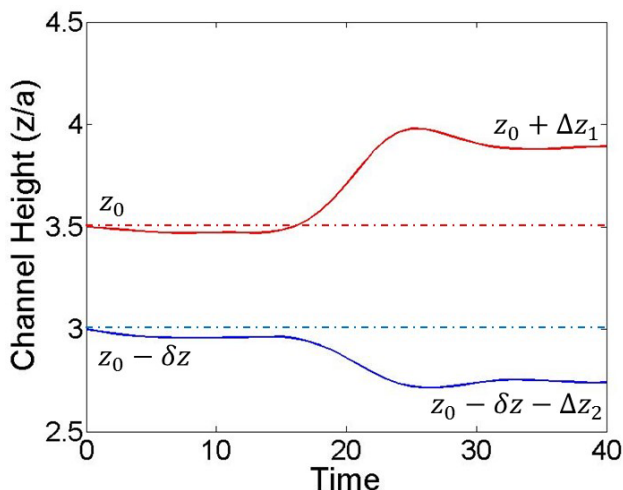
FIG. 7. Sample trajectories from cell-cell simulation after correcting for cell lifting, $L_z = 12(H = 33.8\,\mu\text{m})$, Ca $= 1$, the red line denotes the near-center cell and the blue line denotes the near-wall cell.

B. Collision simulations

Sample trajectories of particles in pair collisions are shown in Figs. 7 and 8. We observed trajectories similar to those for drops [61], capsules [44], and red blood cells [45] in simple shear flow. In unbound, free shear studies, the Δ values are identical for two particles due to symmetry. In bound, pressure-driven flow, however, the collisions are always asymmetric due to wall effects as well as the varying shear rate. Comparing cell-cell collisions to platelet-platelet collisions, Δ_{CC} are slightly bigger as a net result of the particle size and deformability. All else being equal, the displacement value increases with particle size. More deformable particles have smaller displacement values at small δ_z and δ_y due to the ability of two cells to change configuration and affect the flow
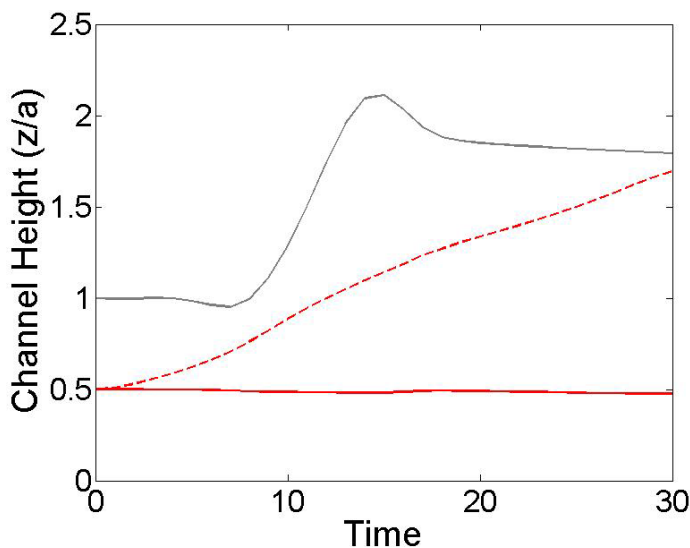

FIG. 8. Sample trajectories from cell-platelet collision, $L_z = 12$ ($H = 33.8\,\mu\text{m}$), Ca $= 1$, gray line denotes near-center platelet trajectory, red dashed line denotes near-wall red blood cell's original trajectory including lift effect, red solid line denotes corrected trajectory.

field. For the interaction between two different types of particles, Δ decreases with both size and deformability. As seen from the sample trajectory plot of cell-platelet interactions in Fig. 8, the red blood cell undergoes a very small change in trajectory. This fact, along with the difference in concentrations, makes the flux of red blood cells due to cell-platelet interactions negligible. Our assumption in master equation (1) is thus confirmed that F_{PC} does not need to be included. Δ_{CP} is the biggest among all types of collisions, and plays a key role in platelet margination. Our findings are consistent with those from other capsule simulations [77,78].

We return to a discussion of the importance the wall effects on cell-cell collisions in wall-bound pressure-driven flow. In order to circumvent the problem of wall-induced red blood cell lifting during collisions, unbound free shear flow simulations have sometimes been used to estimate the Δ values [44,45] and these obviously do not take into account the wall effects. Alternatively, Narsimhan *et al.* simulated two red blood cells near a wall in simple shear flow and determined the Δ values by subtracting the lift trajectory from the actual trajectory. They found the near-wall Δ values deviate from the far-field estimation especially when δ_z is small. More specifically, the wall prevents cells from getting closer to the wall after collisions by changing the force dipole in the flow. Similar observations have been made for rigid spheres in shear flow [46,79] and are said to enhance particle layering in polydisperse solutions. In our work for the pressure-driven flow, we also find significant wall effects even when δ_z values are not small and the cells are at moderate proximity to the wall. As shown in Fig. 7, the near-wall cell has a smaller Δ value although it is located more than two cell radii away from the wall. This reduction in displacement value is as if a repulsive force prevents the particles from penetrating through the wall. Another wall effect is observed in cell-platelet binary collision as shown in Fig. 8. The red blood cell, as the near-wall particle, lifts up in the z direction and is unaffected by the presence of the platelet. However, the platelet, not experiencing a lift force, displaces over an $O(a)$ distance. This big displacement can be explained by the fact that there exists a velocity difference in both the x and z directions for the two approaching particles. Near the wall, the z component of relative velocity is significant and thus makes an additional contribution to the cross-stream displacement Δ. This secondary effect from wall-induced lift makes the collision asymmetric and affects the distribution of red blood cells and platelets. In addition, the difference in size between red blood cells and rigid particles provides a distinct minimum distance to the wall, which is important in the examination of near-wall particle distributions.

We examine the dependence of the collisional displacements on z, δ_z, and δ_y. It makes physical sense that the displacement values decrease with the increase in δ_z and δ_y. In simple shear flow, it has been found that hydrodynamic interactions are negligible for $\delta_z > 5, \delta_y = 0$ [45]. Here we report a cut-off value of $\delta_z > 3, \delta_y = 0$, which is lower due to the reduced shear rate away from the wall. Therefore, we use $R = 3$ as a cutoff distance in the integral calculation for collisional flux calculations. The δ_y dependence is ignored in some previous studies [46,77] in shear flow—in other words, shear-induced diffusion is assumed to be two-dimensional only. We find significant variation in the collisional displacement Δ for δ_y up to 2.0. Thus, a two-dimensional model would underestimate the hydrodynamic interactions and result in a lower diffusional flux. This would affect predictions of the cell-free layer thickness.

The dependence of Δ on z is important and we carefully investigate it in this work. In addition to the wall effect mentioned above, the varying shear rate significantly affects cross-flow movements as well. As shown in Fig. 9, there is not a monotonic correlation of Δ vs. z, and we discuss these results from a qualitative physical perspective. For a near-center RBC as seen in Fig. 9(a), the minimum distance is at least 1.5 cell size away from the wall and therefore there are no available data for Δ at very small z values. Δ is large and constant when $z < 5$ where it remains a saturated ellipsoidal shape at high shear rates. When z increases and this near-center cell changes to a slipperlike shape at reduced shear rates [14], Δ decays quickly. For the near-wall cell in Fig. 9(b), Δ is zero at closest distance to wall, reaches maximum between the wall and the center and drops again near the center. As mentioned before, the collisions are asymmetric and z is defined with respect to the final position. Thus, for small δ_z, Δ values are roughly the same for the near-wall and near-center particles at equal z.
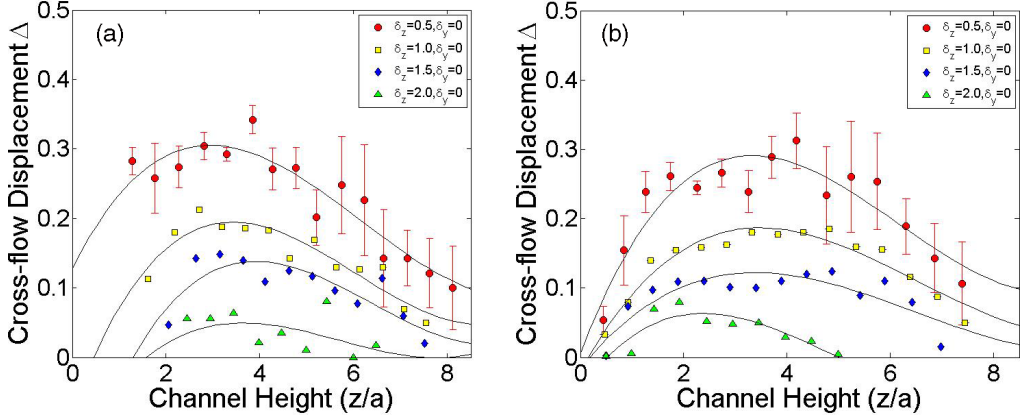
FIG. 9. Cross-flow displacement Δ values vs. z positions from cell-cell collision simulations, (a) near-center cell, (b) near-wall cell, $L_z = 17.73$ ($H = 50\ \mu$m), Ca $= 1$, $\delta_z = 0.5$, $\delta_y = 0$ (spheres), $\delta_z = 1$, $\delta_y = 0$ (squares), $\delta_z = 1.5$, $\delta_y = 0$ (diamonds), $\delta_z = 2$, $\delta_y = 0$ (triangles).

The effect of capillary number on Δ is examined in Fig. 10. We take the ratio of Δ at different capillary numbers to that at Ca $= 1$ and then average over the whole range of z, δ_z and δ_y values to report a general trend of Δ vs. Ca. Thus, we observe an increase of Δ with Ca, which is most obvious between Ca $= 0.25$ and Ca $= 0.5$. Above Ca $= 0.5$, Δ values remain almost constant. As pointed out by Zhao *et al.* [54], Ca $= 0.5$ is the onset of tank-treading behavior of red blood cells. Therefore, the flow field is strong enough to fully deform the cell and the cross-flow movement is no longer sensitive to the capillary number. The weak increase of Δ at higher Ca may arise from the shorter interaction time.

IV. RESULTS: THEORY

A. Red blood cell migration profile

We first solve Eq. (1) with $D = 0$ and examine the effect of the nonlocal shear rate correction term κ as shown in Fig. 11. A $\kappa = 1$ correction effectively imposes a simple shear flow that is of the same
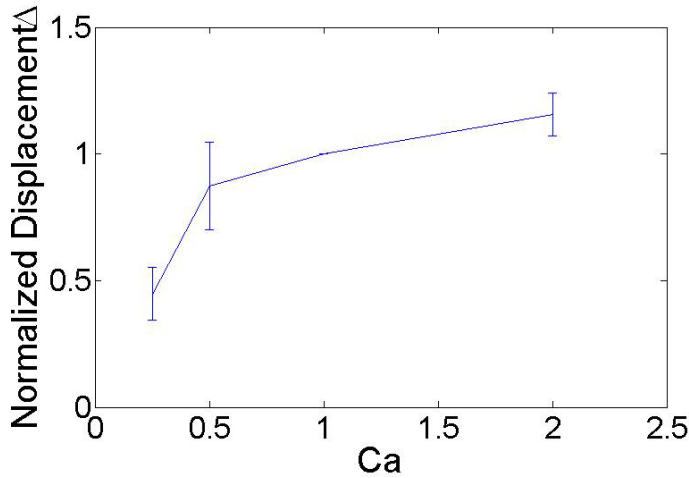

FIG. 10. Average cross-flow displacement Δ normalized by the average value at Ca $= 1$ vs. Ca from cell-cell collision simulations, $L_z = 17.73$ ($H = 50\ \mu$m).
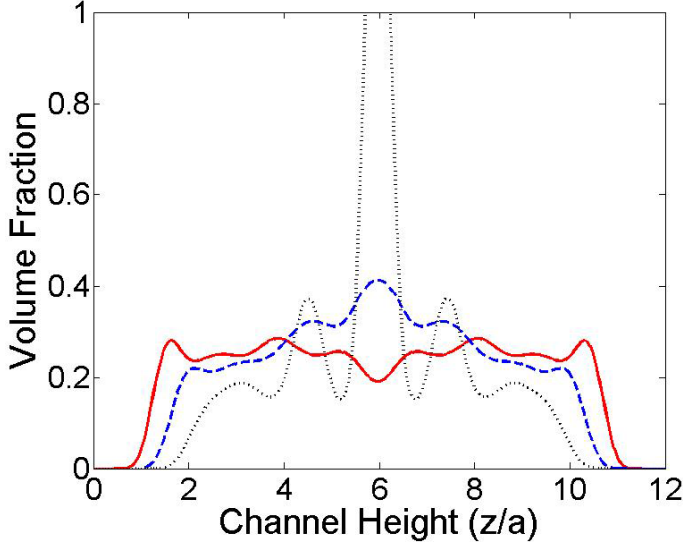
FIG. 11. Nonlocal shear rate effect on red blood cell concentration distribution, $\kappa = 1$ (red solid), ϵ (blue dashed), ϵ^2 (black dotted), $D = 0$, $L_z = 12$ ($H = 33.8 \, \mu$m), Ht = 20%, Ca = 1.

order of magnitude as the actual pressure-driven flow. Therefore, the correction term dominates in the bulk region except near the wall, and the red blood cell concentration profile no longer has a peak concentration at the centerline, characteristic of shear-induced diffusion in a pressure-driven flow. The profile thus looks similar to that obtained for the wall-bound, simple shear flow case [45]. When $\kappa = \epsilon^2$, the correction term is so small that the volume fraction of red blood cells exceeds the maximum packing of 1 at the center. Therefore, the singularity is not eliminated. We conclude that $\kappa = \epsilon$ gives the best correction, which effectively brings down the concentration peak while not affecting the bulk region. Our choice of κ is consistent with previous work on spheres in a pressure-driven flow [3]. This effect can be interpreted as RBCs experiencing the volume average of the positive shear rate over a red blood cell at the centerline and is a nontrivial correction only near the center as compared to the effect of the center-of-mass shear rate $\dot{\gamma}_0$.

The term D corresponding to higher-order (multiparticle) collisions acts as an additional shear-induced diffusive effect, and tends to smooth the concentration distribution of red blood cells. We compare our theoretical results to those from large-scale simulations as in Fig. 12. As mentioned before, the dimensional diffusivity D scales linearly with $\dot{\gamma}$, and thus is greatest at the wall and can affect the cell-free layer thickness. We quantify the cell-free layer thickness by identifying the first concentration peak from the wall and subtracting half the z dimension of the cell as shown in Fig. 13. After fitting, we have matched cell-free layer thicknesses l with those from large-scale simulation at Ca = 1 within 1% error. The fitted dimensionless diffusivity $\bar{D}$ increases from 0.006 at Ht = 10% to 0.014 at Ht = 20%, and reaches 0.02 at Ht = 30%. This trend agrees with the fact that higher-order collisions occur more frequently at higher concentrations. The exact correlation between $\bar{D}$ and Ht is not clear from three data points. We have calculated the relative error in cell-free layer calculation associated with the effect of D in Fig. 14. Even in the case of $D = 0$, our theoretical results are very close to the simulation results. This good agreement proves our assumption (iii) that binary interactions dominate shear-induced diffusion for the hematocrits that we are investigating. The best-fit D values, however do reduce the relative error to be within the tolerance of discretization. Therefore, we consider D as an optional parameter to fine-tune our results for better agreement.

The effect of hematocrit on red blood cell concentration distribution is shown in Fig. 12 and 13. When the hematocrit doubles from 10% to 20%, the volume fraction of red blood cells does not
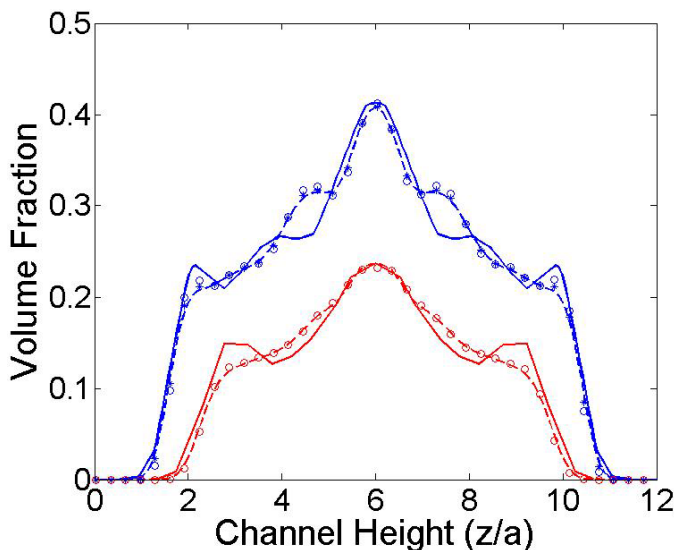
FIG. 12. Comparison of red blood cell concentration distribution between large-scale simulation (solid) and theoretical results at various $\bar{D}$ values, at Ht = 20% (blue) and Ht = 10% (red), $L_z = 12$ ($H = 33.8\ \mu$m), Ca = 1. At Ht = 20%, $\bar{D} = 0$ (circles), 0.007 (crosses), 0.014 (dashed line). At Ht = 10%, $\bar{D} = 0$ (circles), 0.006 (dashed line).

increase consistently at each location. In fact, the cell-free layer thickness l decreases as hematocrit changes from 10% to 20%, and thus the center peak concentration does not double. We can make a simple scaling argument regarding the hematocrit effect: the lift flux scales linearly with ϕ_C, but the collisional flux scales quadratically with ϕ_C. Therefore, the hydrodynamic lift becomes relatively weak at higher hematocrit, and it follows that the cell-free layer thickness is smaller. Katanov *et al.* provided an alternative explanation using the balance of surface pressure and arrived at the same
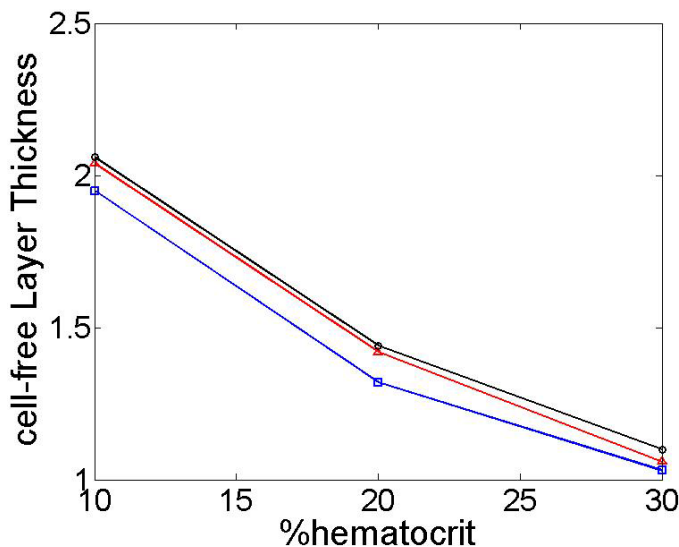

FIG. 13. Cell-free layer thickness l at various hematocrits, using $D = 0$ (blue squares), D at best fit (red triangles) and simulations (black spheres), $L_z = 12$ ($H = 33.8\ \mu$m), Ca = 1.
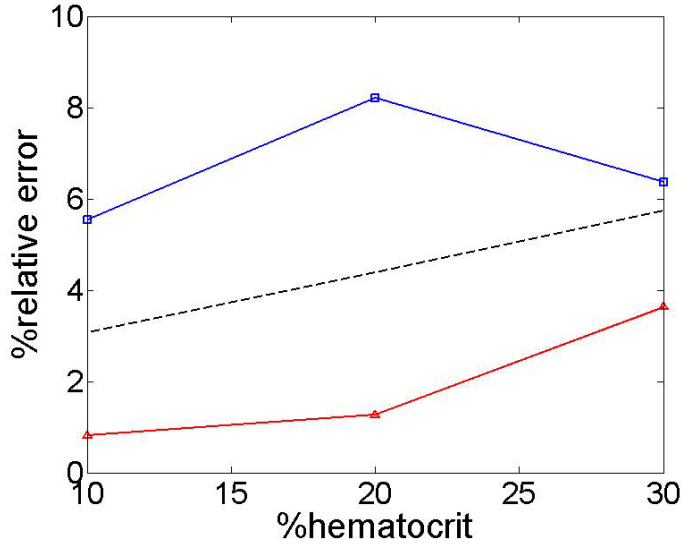
FIG. 14. Relative error in cell-free layer thickness at various hematocrits, using $D = 0$ (blue squares), D at best fit (red triangles), and the discretization error (black dashed line), $L_z = 12(H = 33.8\,\mu\text{m})$, Ca = 1.

conclusion for the effect of hematocrit in tubes whose radius is smaller than those considered in our study [39]. Narsimhan *et al.* found that $l \sim \phi_C^{-1/2}$ for simple shear flow [45]. Our results follow a similar trend in pressure-driven flow because the near-wall region resembles that of simple shear flow. Notice that the effect of the hematocrit on the cell-free layer thickness is expected to saturate at higher hematocrits, e.g., 40%.

A comparison of the RBC concentration distribution in pressure-driven flow and shear flow [45] at equal capillary number is shown in Fig. 15. As mentioned previously, the peak concentration in pressure-driven flow occurs at the centerline due to the zero shear rate while the peak is close to the
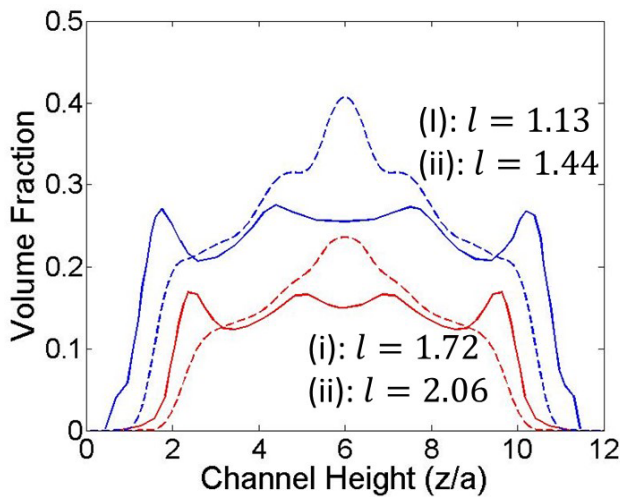

FIG. 15. Red blood cell concentration distribution at Ht = 20% (blue) and Ht = 10% (red) for simple shear flow [(i), solid] and pressure-driven flow [(ii), dashed], cell-free layer thicknesses l are labeled, $L_z = 12\,(H = 33.8\,\mu\text{m})$, Ca = 1.
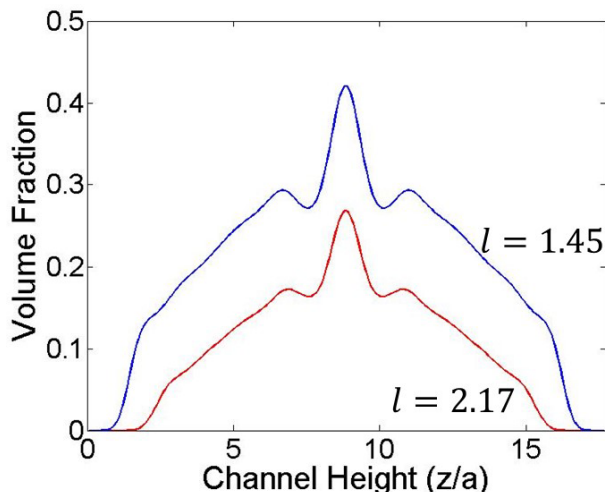
FIG. 16. Red blood cell concentration profile at Ht = 20% (blue) and Ht = 10% (red), cell-free layer thicknesses l are labeled, $L_z = 17.73$ ($H = 50\,\mu$m), Ca = 1.

cell-free layer in simple shear flow due to the balance between near-wall lift and collisions. We find the cell-free layer thickness to be 20% smaller (all else being equal) in simple shear flow. While the lift flux and collisional fluxes are roughly the same in both cases for the near-wall region at matching shear rate, their differences become significant away from the wall. Both the collisional frequency and the displacement values in pressure-driven flow are lower due to the reduced shear rate. Therefore, shear-induced diffusion is weaker, and red blood cells are more likely to be concentrated near the centerline.

We consider channel width of both 30 μm and 50 μm in our theory. The good agreement between our theory in the 30 μm channel with large-scale simulation gives us confidence in the accuracy of our 50 μm channel theory. As seen in Fig. 16, the distribution of red blood cells in a 50 μm channel in general resembles the profile of 30 μm being stretched to 50 μm, with a slight increase in the cell-free layer thickness. This effect is as expected because both lift flux and collisional flux depend weakly on the channel width.

Finally, we examine the variation of the cell-free layer thickness with the capillary number. Using diffusivity values $\bar{D}$ fitted for Ca = 1 at different capillary numbers as seen in Fig. 17, we find that the cell-free layer thickness does not change significantly with the capillary number, which is similar to our previous findings in simple shear flow [45]. This result can be easily explained by the fact that the lift flux and velocity scale linearly with the shear rate. The collisional displacement Δ does not change significantly with the shear rate, but the collision frequency is proportional to the shear rate. Thus, collisional flux also scales nearly linearly with the shear rate. The balance between lift flux and collisional flux is therefore independent of the shear rate. The importance of red blood cell migration lies in generating a cell-free layer where platelets accumulate. From the above discussion, we can see that the cell-free layer thickness is more influenced by hematocrit than the capillary number, and therefore we would expect hematocrit to play a key role in platelet margination as well. We note that, at small capillary numbers, the flow strength will still play an important role in determining the cell-free layer thickness, as can be seen from the work by Katanov and coworkers [39]. They observed an increase of the cell-free layer thickness with capillary number at small Ca, i.e., values much smaller than those investigated herein.

B. Platelet margination profile

Using the red blood cell concentration profile we have calculated, we obtain the platelet concentration profile as shown in Figs. 18, 19, and 20 along with experimental results in which
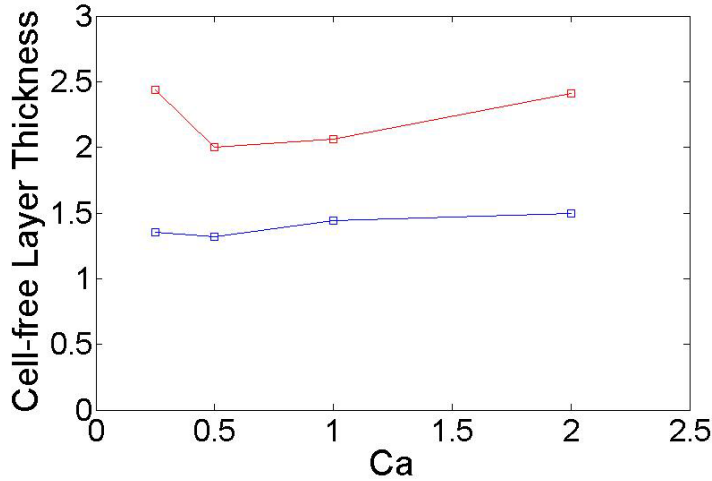
FIG. 17. Cell-free layer thickness l at Ht = 20% (blue) and Ht = 10% (red), $L_z = 12$ ($H = 33.8$ μm).

platelet-sized spheres were employed at matching n_P [6,15]. We find good agreement between theory and experiments. The slight discrepancies can be attributed to experimental errors and the difference in particle shapes [37]. We demonstrate that platelets marginate to the near-wall region where a cell-free layer is formed. Considering the fact that the volume fractions of both the spheres used in the experiments and the platelets in whole blood are at least an order of magnitude lower than that of red blood cells, we ignore the higher-order collisional effects as we did for red blood cells and thus there are no fitting parameters in obtaining the platelet margination profile. Zhao *et al.* calculated the diffusivity of platelets from pressure-driven flow simulations [14]. They characterized platelet margination as caused by shear-induced diffusion in the cell-laden region as well as an
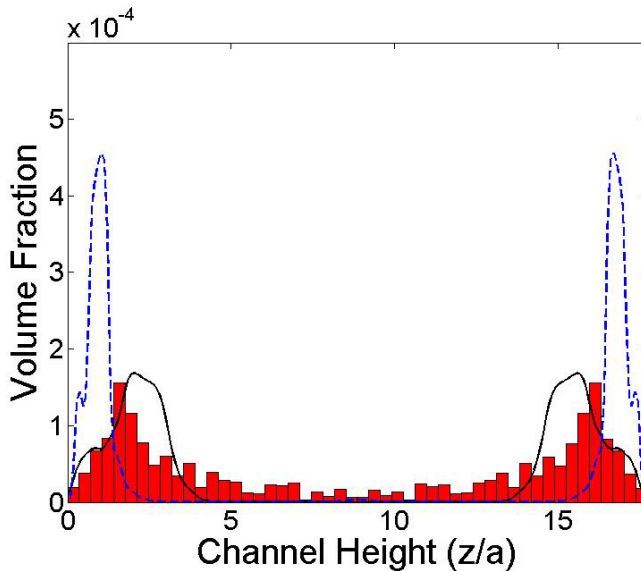

FIG. 18. Platelet concentration profile using experiments [6] (red histogram) at Ht = 10%, and theories(lines) at Ht = 10% (black solid) and Ht = 20% (blue dashed), $L_z = 17.73$ ($H = 50$ μm), Ca = 0.5.
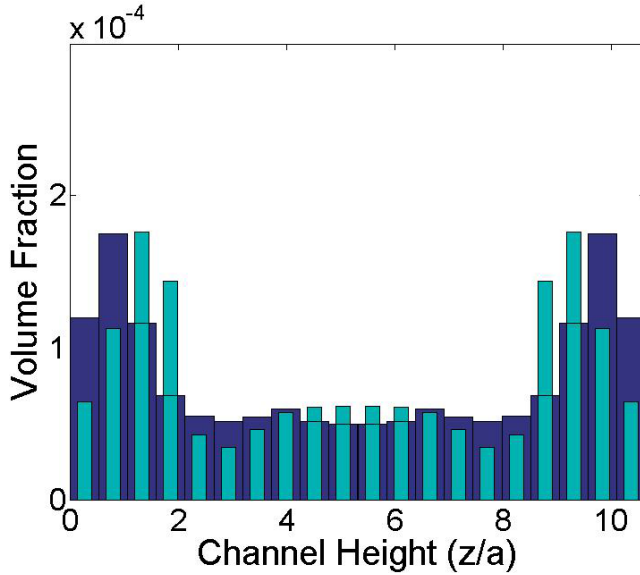
FIG. 19. Platelet concentration profile using experiments [15] (dark blue) at Ht $= 10\%$, and theories (light blue) at Ht $= 10\%$, $L_z = 10.63$ ($H = 30\ \mu$m), Ca $= 0.41$.

irreversible drift towards the cell-free layer. This drift is caused by asymmetric collisions with red blood cells close to the wall. Vahidkhah $et\ al.$ [80] reported similar types of behavior in simple shear flow simulations and characterized platelets' movement in the cell-laden region as a slow process while the movement towards the cell-free layer as a fast process. In our Boltzmann-like formulation of the cell-platelet collisional flux, the drift effect can be seen due to the decoupled red blood cell
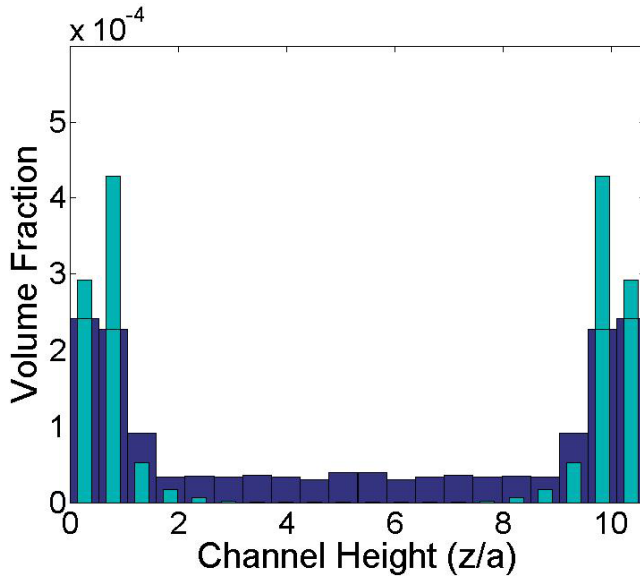

FIG. 20. Platelet concentration profile using experiments [15] (dark blue) at Ht $= 20\%$, and theories (light blue) at Ht $= 20\%$, $L_z = 10.63$ ($H = 30\ \mu$m), Ca $= 0.36$.

concentration profile. At the edge of the cell-free layer, a steep change in cell concentration causes a gradient in collisional frequency. Therefore, a platelet is pushed towards the wall. On the other hand, the increase in platelet collisional displacement due to red blood cell lifting, as seen in Fig. 8, serves as a barrier when a platelet in the bulk region approaches the edge of the cell-free layer and slows down shear-induced diffusion. Thus, our model successfully captures the mechanism by which platelets aggregate in the cell-free layer without using large-scale simulation.

The effect of hematocrit on particle margination is shown in Fig. 18. At a higher hematocrit, the platelet concentration peak is closer to the wall with a higher peak value, meaning that platelets are more aggregated in the cell-free layer. From 10% to 20% hematocrit, the platelet concentration peak is shifted by 2.3 μm. There are two reasons for this trend. The higher hematocrit increases the cell-platelet collisional frequency, and thus the stronger shear-induced diffusion and drift drive more particles into the cell-free layer. Furthermore, the higher hematocrit leads to a smaller cell-free layer thickness. Thus, the location of this peak is shifted. As mentioned previously, the near-wall concentration of platelets is closely related to the time for starting a clot. Within a reactive distance of 200 nm [32,81], we estimate that the platelet concentration doubles from 10% to 20% hematocrit. Thus, we have shown the role of hematocrit on platelet margination, and in future studies, we plan to introduce platelet adhesion to our model as an additional flux term and relate hematocrit to bleeding as shown by Valeri's experiment [12].

Previous literature on particle margination usually ignores platelet-platelet collisions by arguing that the low concentration of platelets makes their interactions trivial. Mehrabadi *et al.* considers platelet concentration in the cell-free layer as a flux from the bulk region exiting a free-escape boundary [26]. Rivera *et al.* included only cell-platelet interactions and predicted a step function of platelet concentration with a constant value in the cell-free layer and zero concentration in the cell-laden region [47,58]. While these results are qualitatively correct, we include the effect of F_{PP} to achieve good quantitative results in the cell-free layer. This effort is important especially since hemostasis requires a close examination of the near-wall region. As mentioned before, the difference in size between red blood cells and rigid particles creates a region in which the particles can exist but red blood cells do not. Thus, the cell-platelet collisional flux in this region is always zero, leading to singular concentrations in the absence of other physics. It is necessary that we consider platelet-platelet collisions so that we obtain a well-defined platelet concentration profile, even though this flux term is, in general, negligible in the presence of red blood cells.

C. Rigid sphere margination profile

We show the theoretically predicted margination profile for spheres of diameter 10 nm, 100 nm, and 1 μm in Fig. 21. The results of 100 nm and 1 μm spheres do not significantly differ, indicating that Brownian motion does not play a significant role in the particle distribution. For 10 nm spheres, the concentration peak inside the cell-free layer is reduced by half, indicating that Brownian motion contributes a flux that is comparable to the other two flux terms. However, the concentration peak is still evident, indicating the existence of margination for such sized nanoparticles. Rivera *et al.* also considered Brownian effects in their theory for rigid trace particles in capsule suspensions [58]. Similar to our findings, the addition of Brownian diffusivity weakens the particle margination in terms of the cumulative concentration of these particles inside the cell-free layer. In both theories, Brownian motion was not accounted for in hydrodynamic collisions because the displacements were of the same size as that for bigger spheres. Notice that we did not include Brownian motion in a collision in this theory: we assumed the displacements were of the same size as those for bigger particles. This is a significant assumption, essentially it assumes that the shear rate is high during a collision and the associated Peclet number is large. Our results are also consistent with the findings that microspheres are more marginated than nanoparticles, which may be related to drug delivery efficiency [82]. Müller *et al.* [5] points out that this concentration peak may eventually decrease to a saturated value for strong Brownian motion where particles will distribute evenly in the cell-free
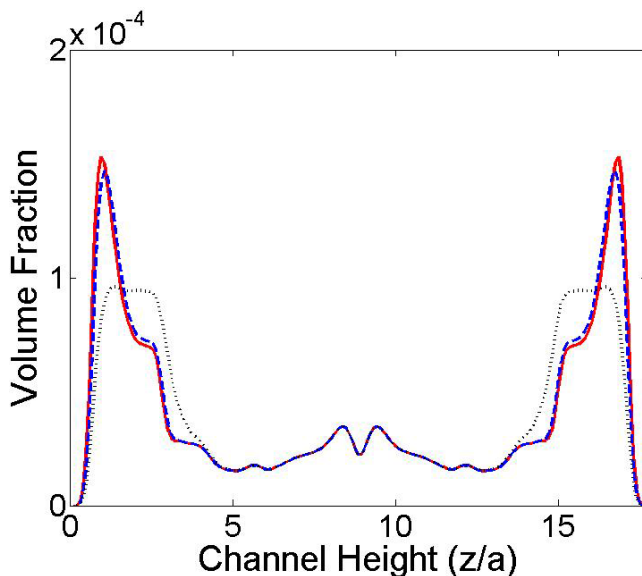
FIG. 21. Concentration profile for spheres of diameter 1 μm (red solid), 100 nm (blue dashed), and 10 nm (black dotted), Ht = 10%, $L_z = 17.73$ ($H = 50$ μm), Ca = 1.

layer and the cell-excluded volume in the bulk region. In this limit, Brownian motion dominates shear-induced diffusion and red blood cells may exert only a volume-exclusion effect.

From the above discussion, we note another advantage of using coarse-grained theory: since red blood cell migration is decoupled from particle margination, we can quickly predict margination behavior for any given red blood cell concentration profile without running multiple sets of large-scale simulations.

V. CONCLUSIONS

In this paper, we study red blood cell migration as well as rigid particle margination in pressure-driven flow through rectangular capillaries at zero Reynolds number. We develop a coarse-grained theory to predict the concentration distribution of the deformable cells and rigid particles, which can be solved via flux balances in the cross-flow direction. Three types of fluxes govern the cross-flow distributions of red blood cells and rigid particles: hydrodynamic lift, hydrodynamic collisions and fluctuations, and Brownian motion. Red blood cells, occupying the largest volume and having deformable and aspherical shapes, are governed by the balance between hydrodynamic lift and cell-cell interactions. Rigid- oblate-shaped platelets occupy a very small volume fraction and are influenced by both cell-platelet interactions and platelet-platelet interactions. Finally, for rigid μm-sized or nanosized spheres, Brownian motion is considered in addition to hydrodynamic interactions.

We calculate flux terms using inputs from simulations of one or two particles, and thus save a significant amount of computation as compared to whole blood simulation. We characterize the lift velocity of a red blood cell in pressure-driven flow, which results from both a wall effect as well the flow curvature. This lift velocity creates a convective flux, which is the fundamental cause of the Fahraeus-Lindqvist effect. The binary collisions, along with higher-order collisions, have a diffusive effect commonly known as shear-induced diffusion. We obtain the increase in relative distance between two particles due to hydrodynamic interactions. These displacement values depend on the type of particles as well as the absolute and relative positions of particles. We also introduce a nonlocal shear rate correction term to the continuum model in order to resolve concentration

at the centerline of the channel, which would be undefined due to zero local shear rate in simple shear-induced diffusion models.

Our theory successfully predicts the peak concentration of red blood cells at the centerline and a cell-free layer near the wall. A comparison to whole blood simulation shows good qualitative and near-quantitative agreement, which is a significant improvement over existing simplified models. We also estimate the peak concentration of rigid particles in the cell-free layer in comparison to experimental data. We examine the effect of particle size on particle margination in flowing blood, and demonstrate that the margination is still evident for 10 nm particles, despite the effects of Brownian motion.

We choose parameters in the physiological range to present our results and estimates. Thus, our theory builds a practical model for understanding blood suspensions and designing microfluidic devices. Red blood cells are the dominant species in blood and their migration can, under certain circumstances, be decoupled from the motion of more rigid, smaller particles. Therefore, we can study the effects of various sizes and shapes of particles at a fixed hematocrit independently without revisiting the red blood cell migration. Our model can serve as a blueprint for solving transport problems in cellular suspensions and is a good alternative to large-scale computer simulation.

ACKNOWLEDGMENTS

---

[1] P. A. Aarts, S. A. van den Broek, G. W. Prins, G. D. Kuiken, J. J. Sixma, and R. M Heethaar, Blood platelets are concentrated near the wall and red blood cells, in the center in flowing blood, Arterioscler Thromb Basc Biol. **8**, 819 (1988).

[2] R. Fahreus and T. Lindqvist, The viscosity of the blood in narrow capillary tubes, Am. J. Phys. **96**, 562 (1931).

[3] R. M. Miller and J. F. Morris, Normal stress-driven migration and axial development in pressure-driven flow of concentrated suspensions, J. Non-Newtonian Fluid Mech. **135**, 149 (2006).

[4] G. J. Tangelder, H. C. Teirlinck, D. W. Slaaf, and R. S. Reneman, Distribution of blood platelets flowing in arterioles, Am. J. Physiol.: Heart Circ. Physiol. **248**, H318 (1985).

[5] K. Müller, D. A. Fedosov, and G. Gompper, Margination of micro- and nano-particles in blood flow and its effect on drug delivery, Sci. Rep. **4**, 4871 (2014).

[6] R. D'Apolito, G. Tomaiuolo, F. Taraballi, S. Minardi, D. Kirui, X. Liu, A. Cevenini, R. Palomba, M. Ferrari, F. Salvatore *et al.*, Red blood cells affect the margination of microparticles in synthetic microcapillaries and intravital microcirculation as a function of their size and shape, J. Controlled Release **217**, 263 (2015).

[7] R. Toy, E. Hayden, C. Shoup, H. Baskaran, and E. Karathanasis, The effects of particle size, density and shape on margination of nanoparticles in microcirculation, Nanotechnology **22**, 115101 (2011).

[8] N. Doshi, B. Prabhakarpandian, A. Rea-Ramsey, K. Pant, S. Sundaram, and S. Mitragotri, Flow and adhesion of drug carriers in blood vessels depend on their shape: A study using model synthetic microvascular networks, J. Controlled Release **146**, 196 (2010).

[9] A. R. Pries, D. Neuhaus, and P. Gaehtgens, Blood viscosity in tube flow: Dependence on diameter and hematocrit, Am. J. Physiol.: Heart Circ. Physiol. **263**, H1770 (1992).

[10] T. W. Secomb, Hemodynamics, Comprehensive Physiology **9**, 975 (2016).

[11] V. Jonsson, J. E. Bock, and J. B. Nielsen, Significance of plasma skimming and plasma volume expansion, J. Appl. Physiol. **72**, 2047 (1992).

[12] C. R. Valeri, G. Cassidy, L. E. Pivacek, G. Ragno, W. Lieberthal, J. P. Crowley, S. F. Khuri, and J. Loscalzo, Anemiainduced increase in the bleeding time: Implications for treatment of nonsurgical blood loss, Transfusion **41**, 977 (2001).

[13] M. Mehrabadi, Effects of red blood cells and shear rate on thrombus growth, Doctoral dissertation, Georgia Institute of Technology, 2014.

[14] H. Zhao, E. S. G. Shaqfeh, and V. Narsimhan, Shear-induced particle migration and margination in a cellular suspension, Phys. Fluids **24**, 011902 (2012).

[15] S. Fitzgibbon, A. P. Spann, Q. M. Qi, and E. S. G. Shaqfeh, In vitro measurement of particle margination in the microchannel flow: Effect of varying hematocrit, Biophys. J. **108**, 2601 (2015).

[16] A. P. Spann, J. E. Campbell, S. R. Fitzgibbon, A. Rodriguez, A. P. Cap, L. H. Blackbourne, and E. S. G. Shaqfeh, The effect of hematocrit on platelet adhesion: Experiments and simulations, Biophys. J. **111**, 577 (2016).

[17] M. Abkarian and A. Viallat, Vesicles and red blood cells in shear flow, Soft Matter **4**, 653 (2008).

[18] P. B. Canham and A. C. Burton, Distribution of size and shape in populations of normal human red cells, Circ. Res. **22**, 405 (1968).

[19] G. Tomaiuolo, M. Simeone, V. Martinelli, B. Rotoli, and S. Guido, Red blood cell deformation in microconfined flow, Soft Matter **5**, 3736 (2009).

[20] N. Mohandas and J. A. Chasis, Red blood cell deformability, membrane material properties and shape: Regulation by transmembrane, skeletal and cytosolic proteins and lipids, in *Seminars in Hematology*, Vol. 30 (1993), pp. 171–192.

[21] G. Tomaiuolo, Biomechanical properties of red blood cells in health and disease towards microfluidics, Biomicrofluidics **8**, 051501 (2014).

[22] Z. Peng, X. Li, I. V. Pivkin, M. Dao, G. E. Karniadakis, and S. Suresh, Lipid bilayer and cytoskeletal interactions in a red blood cell, Proc. Natl. Acad. Sci. USA **110**, 13356 (2013).

[23] Y. Suzuki, N. Tateishi, M. Soutani, and N. Maeda, Flow behavior of erythrocytes in microvessels and glass capillaries: Effects of erythrocyte deformation and erythrocyte aggregation, Int. J. Microcirculat. **16**, 187 (1996).

[24] D. A. Fedosov, B. Caswell, and G. E. Karniadakis, Systematic coarse-graining of spectrin-level red blood cell models, Comput. Methods Appl. Mech. Eng. **199**, 1937 (2010).

[25] D. Rubenstein, W. Yin, and M. D. Frame, *Biofluid Mechanics: An Introduction to Fluid Mechanics, Macrocirculation, and Microcirculation* (Academic Press, New York, 2015).

[26] M. Mehrabadi, D. N. Ku, and C. K. Aidun, A continuum model for platelet transport in flowing blood based on direct numerical simulations of cellular blood flow, Ann. Biomed. Eng. **43**, 1410 (2015).

[27] S. Huang, H. W. Hou, T. Kanias, J. T. Sertorio, H. Chen, D. Sinchar, M. T. Gladwin, and J. Han, Towards microfluidic-based depletion of stiff and fragile human red cells that accumulate during blood storage, Lab on a Chip **15**, 448 (2015).

[28] J. Tan, A. Thomas, and Y. Liu, Influence of red blood cells on nanoparticle targeted delivery in microcirculation, Soft Matter **8**, 1934 (2012).

[29] T. M. Geislinger and T. Franke, Hydrodynamic lift of vesicles and red blood cells in flowfrom fåhræus & lindqvist to microfluidic cell sorting, Adv. Colloid Interface Sci. **208**, 161 (2014).

[30] H. W. Hou, L. Wu, D. P. Amador-Munoz, M. P. Vera, A. Coronata, J. A. Englert, B. D. Levy, R. M. Baron, and J. Han, Broad spectrum immunomodulation using biomimetic blood cell margination for sepsis therapy, Lab on a Chip **16**, 688 (2016).

[31] L. L. Munn and M. M. Dupin, Blood cell interactions and segregation in flow, Ann. Biomed. Eng. **36**, 534 (2008).

[32] S. Fitzgibbon, J. Cowman, A. J. Ricco, D. Kenny, and E. S. G. Shaqfeh, Examining platelet adhesion via stokes flow simulations and microfluidic experiments, Soft Matter **11**, 355 (2015).

[33] F. Gentile, A. Curcio, C. Indolfi, M. Ferrari, and P. Decuzzi, The margination propensity of spherical particles for vascular targeting in the microcirculation, J. Nanobiotechnol. **6**, 9 (2008).

[34] J. Tan, S. Shah, A. Thomas, H. D. Ou-Yang, and Y. Liu, The influence of size, shape and vessel geometry on nanoparticle distribution, Microfluid. Nanofluid. **14**, 77 (2013).

[35] A. Kumar and M. D. Graham, Margination and segregation in confined flows of blood and other multicomponent suspensions, Soft Matter **8**, 10536 (2012).

[36] J. B. Freund and B. Shapiro, Transport of particles by magnetic forces and cellular blood flow in a model microvessel, Phys. Fluids **24**, 051904 (2012).

[37] K. Vahidkhah and P. Bagchi, Microparticle shape effects on margination, near-wall dynamics and adhesion in a three-dimensional simulation of red blood cell suspension, Soft Matter **11**, 2097 (2015).

[38] I. Pivkin, P. Richardson, and G. Karniadakis, *Effect of Red Blood Cells on Platelet Aggregation* (IEEE, Piscataway, 2009).

[39] D. Katanov, G. Gompper, and D. A. Fedosov, Microvascular blood flow resistance: Role of red blood cell migration and dispersion, Microvasc. Res. **99**, 57 (2015).

[40] D. Leighton and A. Acrivos, The shear-induced migration of particles in concentrated suspensions, J. Fluid Mech. **181**, 415 (1987).

[41] P. R. Nott and J. F. Brady, Pressure-driven flow of suspensions: Simulation and theory, J. Fluid Mech. **275**, 157 (1994).

[42] S. D. Hudson, Wall migration and shear-induced diffusion of fluid droplets in emulsions, Phys. Fluids **15**, 1106 (2003).

[43] A. Ramachandran, M. Loewenberg, and D. T. Leighton Jr., A constitutive equation for droplet distribution in unidirectional flows of dilute emulsions for low capillary numbers, Phys. Fluids **22**, 083301 (2010).

[44] K. Sinha and M. D. Graham, Shape-mediated margination and demargination in flowing multicomponent suspensions of deformable capsules, Soft Matter **12**, 1683 (2016).

[45] V. Narsimhan, H. Zhao, and E. S. G. Shaqfeh, Coarse-grained theory to predict the concentration distribution of red blood cells in wall-bounded couette flow at zero reynolds number, Phys. Fluids **25**, 061901 (2013).

[46] M. Zurita-Gotor, J. Bławzdziewicz, and E. Wajnryb, Layering Instability in a Confined Suspension Flow, Phys. Rev. Lett. **108**, 068301 (2012).

[47] Rafael G. Henríquez Rivera, X. Zhang, and M. D. Graham, Mechanistic theory of margination and flow-induced segregation in confined multicomponent suspensions: Simple shear and poiseuille flows, Phys. Rev. Fluids **1**, 060501 (2016).

[48] D. A. Fedosov, B. Caswell, A. S. Popel, and G. E. Karniadakis, Blood flow and cell-free layer in microvessels, Microcirculation **17**, 615 (2010).

[49] R. Skalak, N. Ozkaya, and T. C. Skalak, Biofluid mechanics, Annu. Rev. Fluid Mech. **21**, 167 (1989).

[50] G. J. Tangelder, D. W. Slaaf, A. M. Muijtjens, T. Arts, M. G. Oude Egbrink, and R. S. Reneman, Velocity profiles of blood platelets and red blood cells flowing in arterioles of the rabbit mesentery, Circ. Res. **59**, 505 (1986).

[51] Y. u. Su, R. N. Zia, and J. W. Swan, Does suspension crowding screen hydrodynamic interactions? in APS Meeting Abstracts, Vol. 1 (2015), p. 35006.

[52] R. N. Zia, J. W. Swan, and Y. u. Su, Pair mobility functions for rigid spheres in concentrated colloidal dispersions: Force, torque, translation, and rotation, J. Chem. Phys. **143**, 224901 (2015).

[53] H. H. Lipowsky, S. Kovalcheck, and B. W. Zweifach, The distribution of blood rheological parameters in the microvasculature of cat mesentery, Circ. Res. **43**, 738 (1978).

[54] H. Zhao, A. P. Spann, and E. S. G. Shaqfeh, The dynamics of a vesicle in a wall-bound shear flow, Phys. Fluids **23**, 121901 (2011).

[55] J. R. Smart and D. T. Leighton Jr., Measurement of the drift of a droplet due to the presence of a plane, Phys. Fluids A **3**, 21 (1991).

[56] PC-H. Chan and L. G. Leal, The motion of a deformable drop in a second-order fluid, J. Fluid Mech. **92**, 131 (1979).

[57] M. Marchioro and A. Acrivos, Shear-induced particle diffusivities from numerical simulations, J. Fluid Mech. **443**, 101 (2001).

[58] R. G. H. Rivera, K. Sinha, and M. D. Graham, Margination Regimes and Drainage Transition in Confined Multicomponent Suspensions, Phys. Rev. Lett. **114**, 188101 (2015).

[59] G. Danker, P. M. Vlahovska, and C. Misbah, Vesicles in Poiseuille Flow, Phys. Rev. Lett. **102**, 148102 (2009).

[60] G. Coupier, B. Kaoui, T. Podgorski, and C. Misbah, Noninertial lateral migration of vesicles in bounded poiseuille flow, Phys. Fluids **20**, 111702 (2008).

[61] M. Loewenberg and E. J. Hinch, Collision of two deformable drops in shear flow, J. Fluid Mech. **338**, 299 (1997).

[62] C. Pozrikidis, *Boundary Integral and Singularity Methods for Linearized Viscous Flow* (Cambridge University Press, Cambridge, 1992).

[63] L. Crowl and A. L. Fogelson, Analysis of mechanisms for platelet near-wall excess under arterial blood flow conditions, J. Fluid Mech. **676**, 348 (2011).

[64] J. P. Mills, L. Qie, M. Dao, C. T. Lim, and S. Suresh, Nonlinear elastic and viscoelastic deformation of the human red blood cell with optical tweezers, MCB-Tech Science Press **1**, 169 (2004).

[65] R. E. Waugh and R. M. Hochmuth, Mechanics and deformability of hematocytes, The Biomedical Engineering Handbook **35**, 474 (1995).

[66] H. Hasimoto, On the periodic fundamental solutions of the stokes equations and their application to viscous flow past a cubic array of spheres, J. Fluid Mech. **5**, 317 (1959).

[67] D. Saintillan, E. Darve, and E. S. G. Shaqfeh, A smooth particle-mesh ewald algorithm for stokes suspension simulations: The sedimentation of fibers, Phys. Fluids **17**, 033301 (2005).

[68] L. Shi, T.-W. Pan, and R. Glowinski, Deformation of a single red blood cell in bounded poiseuille flows, Phys. Rev. E **85**, 016307 (2012).

[69] D. S. Hariprasad and T. W. Secomb, Two-dimensional simulation of red blood cell motion near a wall under a lateral force, Phys. Rev. E **90**, 053014 (2014).

[70] P. Olla, The lift on a tank-treading ellipsoidal cell in a shear flow, J. Phys. II France **7**, 1533 (1997).

[71] N. Callens, C. Minetti, G. Coupier, M-A. Mader, F. Dubois, C. Misbah, and T. Podgorski, Hydrodynamic lift of vesicles under shear flow in microgravity, Europhys. Lett. **83**, 24002 (2008).

[72] S. Sukumaran and U. Seifert, Influence of shear flow on vesicles near a wall: A numerical study, Phys. Rev. E **64**, 011916 (2001).

[73] M. Abkarian and A. Viallat, Dynamics of vesicles in a wall-bounded shear flow, Biophys. J. **89**, 1055 (2005).

[74] X. Grandchamp, G. Coupier, A. Srivastav, C. Minetti, and T. Podgorski, Lift and Down-Gradient Shear-Induced Diffusion in Red Blood Cell Suspensions, Phys. Rev. Lett. **110**, 108101 (2013).

[75] B. Kaoui, G. H. Ristow, I. Cantat, C. Misbah, and W. Zimmermann, Lateral migration of a two-dimensional vesicle in unbounded poiseuille flow, Phys. Rev. E **77**, 021903 (2008).

[76] S. Nix, Y. Imai, and T. Ishikawa, Lateral migration of a capsule in a parabolic flow, J. Biomech. **49**, 2249 (2015).

[77] A. Kumar and M. D. Graham, Segregation by membrane rigidity in flowing binary suspensions of elastic capsules, Phys. Rev. E **84**, 066316 (2011).

[78] A. Kumar, R. G. H. Rivera, and M. D. Graham, Flow-induced segregation in confined multicomponent suspensions: Effects of particle size and rigidity, J. Fluid Mech. **738**, 423 (2014).

[79] M. Zurita-Gotor, J. Błaywzdziewicz, and E. Wajnryb, Swapping trajectories: A new wall-induced cross-streamline particle migration mechanism in a dilute suspension of spheres, J. Fluid Mech. **592**, 447 (2007).

[80] K. Vahidkhah, S. L. Diamond, and P. Bagchi, Platelet dynamics in three-dimensional simulation of whole blood, Biophys. J. **106**, 2529 (2014).

[81] K. Bonazza, H. Rottensteiner, B. K. Seyfried, G. Schrenk, G. Allmaier, P. L. Turecek, and G. Friedbacher, Visualization of a protein-protein interaction at a single-molecule level by atomic force microscopy, Anal. Bioanal. Chem. **406**, 1411 (2014).

[82] K. Namdee, A. J. Thompson, P. Charoenphol, and O. Eniola-Adefeso, Margination propensity of vascular-targeted spheres from blood flow in a microfluidic model of human microvessels, Langmuir **29**, 2530 (2013).